Chapter 6: Realization of Upconversion Emission in $Gd_{1-x-y}Yb_xEr_ySc O_3$ Perovskite Nanocrystals for Optical Temperature Sensing Application

6.1 Introduction

In Chapter 3, 4, and 5, properties of $CsPbX_3$ (X=Cl, Br) influenced by different lanthanides are studied. Lanthanide ions are either substituted to one of the host ion or they are present in the framework, such as metal organic framework. This enhances the stability and as well optical properties of the $CsPbX_3$. Lanthanide ion pairs such as Er^{3+}-Yb^{3+}, Ho^{3+}-Yb^{3+}, Tm^{3+}-Yb^{3+}, etc., show peculiar non-linear optical properties called photon upconversion (UC). In these pairs, Yb^{3+}-ion acts as a sensitizer to harvest incident photons and, Er^{3+}, Ho^{3+}, and Tm^{3+}-ions act as an activator. They absorb low enegy Infrared (IR) photons (980 nm) and emit high enegy visible photons. Detailed discussion on UC mechanisms are given in Chapter 1. $CsPbX_3$ thermally unstable, particularly under high temperatures or prolonged exposure to light, which can lead to phase segregation or decomposition. These materials are highly sensitive to moisture, oxygen, and light, leading to degradation over time, which negatively impacts the stability and reliability of UC emission.

Rare-earth scandates materials ($LnScO_3$) have garnered significant interest due to their unique properties, including a high dielectric constant ranging from 22 to 31 [212], a large bandgap between 5.50 and 6.12 eV [213], and excellent high-temperature stability with a melting point around 2100 K [212]. These properties of the $LnScO_3$ making this material suitable for the application such as optical thermometry. In this Chapter, Yb^{3+}, Er^{3+} co-doped $GdScO_3$ nanocrystals (NCs) were synthesized at low temperatures using the self-propagating

gel combustion method. The UC emission properties of Yb^{3+}, Er^{3+} co-doped $GdScO_3$ NCs were investigated for the first time. Hence, demonstrated their potential for non-contact, luminescence-based temperature sensing applications within the temperature range of 299 to 473 K.

6.2 Materials synthesis

6.2.1 Synthesis of $GdScO_3$ nanocrystals

$GdScO_3$ NCs were synthesized by a self-propagated gel-combustion technique [113]. For the synthesis of $GdScO_3$, 4.0 mmol of Gd_2O_3 (99.9%, Alfa Aesar) and 4.0 mmol of Sc_2O_3 (99.99%, Alfa Aesar) were measured and dissolved in a minimal amount of nitric acid (69%, Merck Life Science) to form the corresponding nitrates. The required amount of glycine (99.0%, Thermo Fisher Scientific) was dissolved in 20 ml of deionized water in a 50 ml beaker, and the solution was heated to 150 °C on a hot plate until it became a clear, transparent solution. Glycine was used as a fuel for the combustion reaction. The nitrate of Gd and Sc, and glycine solutions were then mixed in a 500 ml beaker and magnetically stirred at 200 rpm, maintaining the temperature at 150 °C. After approximately 30 minutes, bubbling occurred, and the solution thickened into a gel-like viscous liquid. The temperature was then increased to 250 °C, leading to ignition and the formation of a foam-like white residue. This residue was ground into a fine powder using an agate mortar for further analysis. The resulting $GdScO_3$ powder was then calcined at various temperatures to study the optoelectronic properties.

6.2.2 Synthesis of Yb^{3+}, Er^{3+}: $GdScO_3$ nanocrystal

The synthesis techniques for Er^{3+}-doped $GdScO_3$ and Yb^{3+}, Er^{3+} co-doped $GdScO_3$ NCs are identical to the $GdScO_3$ NCs discussed above. A series of Yb^{3+}, Er^{3+} co-doped $GdScO_3$

samples were synthesized by varying the concentration of Yb (Yb_2O_3, 99.99%, Alfa Aesar) while keeping the concentration of Er (Er_2O_3, 99.99%, Alfa Aesar) fixed. In this $Yb_xEr_yGd_{1-x-y}ScO_3$ series x varies as 0.00, 0.01, 0.03, 0.05, 0.07, and 0.10, with y fixed at 0.005.

6.3 Results and discussion

6.3.1 Structure and morphology

The phase of the synthesized samples were done by the X-ray diffraction (XRD) analysis. The XRD patterns of the samples were obtained using a Miniflex 600 diffractometer from Rigaku, Japan, with a step size of 0.02° over the range of $20° \leq 2\theta \leq 90°$. The diffraction was performed using characteristic wavelength of Cu-Kα radiation of 1.54 Å.

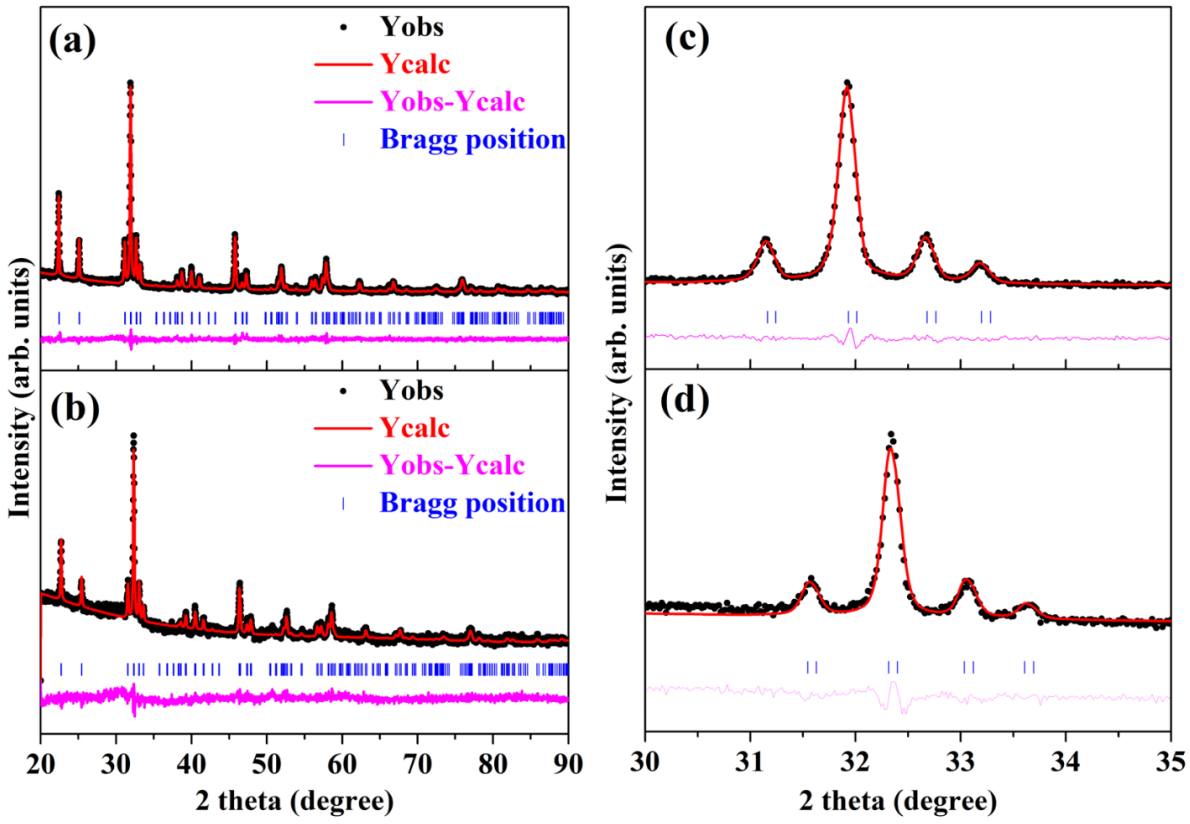

Figure 6.1: Rietveld refined XRD patterns of (a) $GdScO_3$, and (b) $Yb_{0.03}Er_{0.005}Gd_{0.965}ScO_3$ powder sample. Zoomed view of XRD patterns in the range from 30-35° of (c) $GdScO_3$, and (d) $Yb_{0.03}Er_{0.005}Gd_{0.965}ScO_3$ powder sample.

The XRD pattern of synthesized $GdScO_3$ and optimized Yb^{3+}, Er^{3+} co-doped $GdScO_3$ (3.0% Yb^{3+} and 0.5% Er^{3+}) are shown in Fig. 6.1(a) and 6.1(a), respectively. In the $GdScO_3$ XRD pattern major peaks appear at 2θ angle 22.45º, 25.11º, 31.16º, 31.93º, 32.68º, 33.19º, 45.78º, 51.91º, and 57.85º, and corresponding (hkl) values are (101), (111), (200), (121), (002), (210), (202), (311), and (123), respectively. It is in good agreement with the previously reported $GdScO_3$ XRD patterns [214][106][215]. Also Joint Committee on Powder Diffraction Standards (JCPDS) file number 27-0220 confirming an orthorhombic structure with a P*nma* (62) space group.

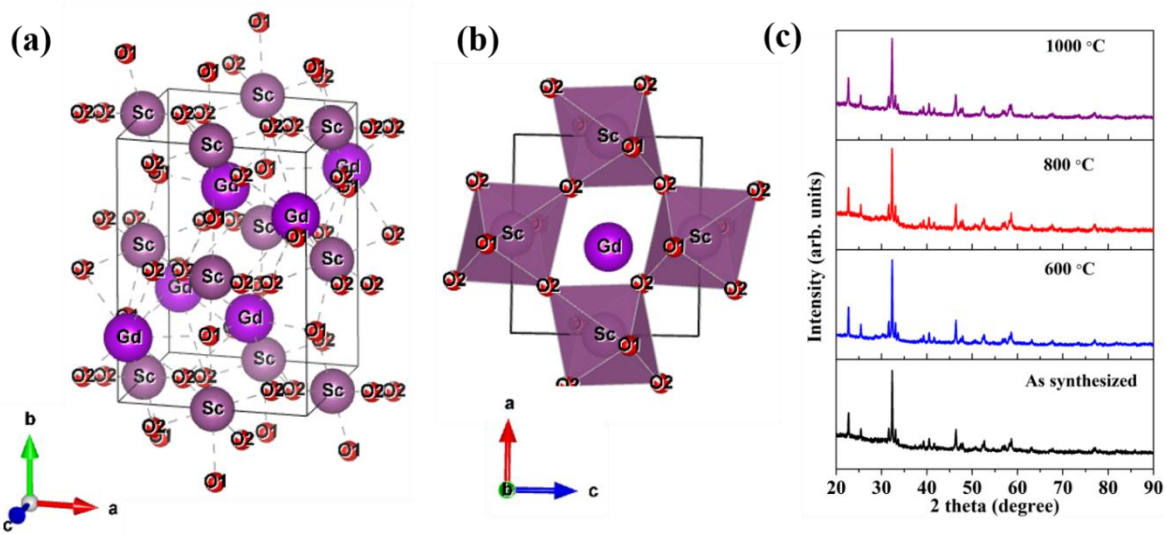

Figure 6.2: (a) The crystal structure of the $GdScO_3$ drawn after Rietveld refinement of XRD data. (b) Octahedra formation of ScO_6. (c) XRD patterns of as-synthesized $Yb_{0.03}Er_{0.005}Gd_{0.965}ScO_3$ sample calcined at 600 ºC, 800 ºC, and 1000 ºC.

The lattice parameters of pristine $GdScO_3$ and optimized Yb^{3+}, Er^{3+} co-doped $GdScO_3$ powder samples, were analyzed using Rietveld refinement via the FullProf Suite software. The refined XRD patterns of $GdScO_3$ and optimized Yb^{3+}, Er^{3+} co-doped $GdScO_3$ powder samples are presented in Fig. 6.1(a) and 1(b), respectively. The refinement parameters and the resulting lattice parameters are summarized in Table 6.1. The lattice parameters of the pristine GdScO3 sample were determined to be a = 5.735(3) Å, b = 7.918(7) Å, and c =

5.475(4) Å, while for the optimized Yb^{3+}, Er^{3+} co-doped $GdScO_3$ sample were found to be *a* = 5.664(7) Å, *b* = 7.820(2) Å, and *c* = 5.414(8) Å. The crystal structure of $GdScO_3$ is depicted in Fig. 6.2(a) [104]. There is slight distortion of the ScO_6 octahedral structure as illustrated in Fig. 6.2(b).

Table 6.1 Rietveld refined lattice parameters of $GdScO_3$ and $Yb_{0.03}Er_{0.005}Gd_{0.965}ScO_3$ XRD data.

Parameters	**$GdScO_3$**	**$Yb_{0.03}Er_{0.005}Gd_{0.965}ScO_3$**
***a* (Å)**	5.7353±0.0002	5.6647±0.0006
***b* (Å)**	7.9187±0.0003	7.8202±0.0009
***c* (Å)**	5.4754±0.0002	5.4148±0.0006
$\alpha = \beta = \gamma$ (º)	90	90
Volume($Å^3$)	248.680±0.018	239.919±0.050
Density ($g.cm^{-3}$)	6.683	7.186
Structure	Orthorhombic	Orthorhombic
Space group	P*nma* (62)	P*nma* (62)
Profile	Pseudo-voigt	Pseudo-voigt
Goodness-of-fit (χ^2)	1.22	1.58
Profile residual (R_p)	2.66	3.72
Weighted profile residual (R_{wp})	3.40	4.72
Expected profile residual (R_{exp})	3.08	3.76

A comparative study of the unit cell parameters after Rietveld refinement of as-synthesized pristine $GdScO_3$ and optimized Yb^{3+}, Er^{3+} co-doped $GdScO_3$ was conducted. The XRD patterns for both samples were recorded at the same scanning rate. All diffraction peaks and their relative intensities for $GdScO_3$ matched well with those of the optimized Yb^{3+}, Er^{3+} co-doped $GdScO_3$, indicating that the phase purity of $GdScO_3$ is maintained even after doping of Er^{3+} and Yb^{3+}-ions. However, a slight shift in the diffraction peaks towards higher

angles was observed in the Yb^{3+}, Er^{3+} co-doped $GdScO_3$ sample as shown in the zoomed images in Fig. 6.1(c) and 6.1(d). This shift is attributed to the lattice contraction upon smaller ionic radii (Yb^{3+} and Er^{3+}) ions doping in place of Gd^{3+} in the $GdScO_3$ [215][216][217]. The lattice contraction due to the Yb^{3+} and Er^{3+}-ions incorporation into the $GdScO_3$ host is also evidenced by the lattice parameters obtained from Rietveld refinementof XRD data. The lattice parameters *a, b, c,* and volume slightly decreased, and an increased density was observed in optimized Yb^{3+}, Er^{3+} co-doped $GdScO_3$ compared to pristine GdScO3, as listed in Table 6.1. The crystallite size of both samples was determined using the Debye-Scherrer equation:

$$D = \frac{0.89\lambda}{\beta\cos\theta} \quad \ldots (6.1)$$

Where D represent the crystallite size, λ is the wavelength of the incident X-ray used in XRD analysis, β represent full-width at half maximum of the diffraction peak, and θ is the position of Bragg's diffraction peak. The average crystallite size calculated for the as-synthesized $GdScO_3$ calculated corresponding to the prominent diffraction peaks is ~49 nm. Whereas, the crystallite size for the optimized Yb^{3+}, Er^{3+} co-doped $GdScO_3$ is around 47 nm. The optimized Yb^{3+}, Er^{3+} co-doped $GdScO_3$ sample is calcined at various temperatures, and cooresponding XRD patterns are displayed in Fig. 6.2(c). The calcined sample is free from some of the organic solvents used while synthesis. Hence which defects get reduced in calcined samples and enhances the crystal purity [218][219]. The crystallinity of the samples get improved after calcination of the sample, that reflect in XRD pattern [220][221][222]. However, the XRD patterns neither show additional peaks in the diffraction pattern nor any shifts in the peak positions after thermal treatment. Additionally, there is no alternation in the intensity of the diffraction peaks, suggesting that the structure and phase are thermally stable.

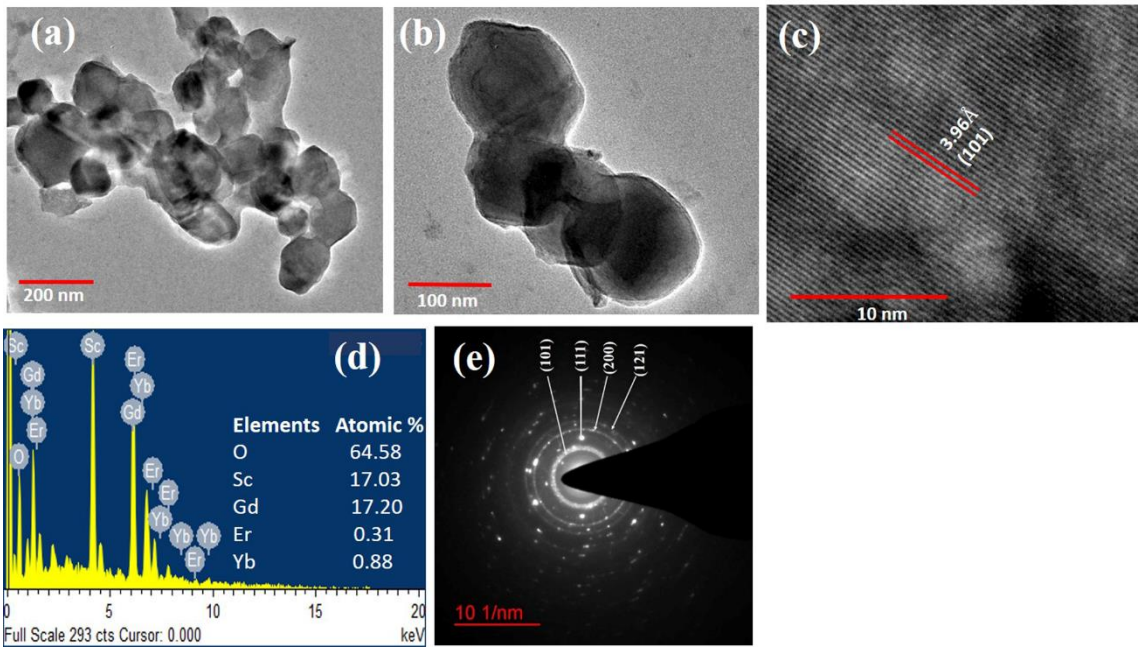

Figure 6.3: (a), (b) TEM images of the powder sample of $GdScO_3$. (c) HRTEM images of the powder sample of $GdScO_3$. (d) Elemental analysis of Yb^{3+}, Er^{3+}: $GdScO_3$ using EDX technique. (e) SAED pattern of $GdScO_3$.

The morphology of the as-prepared $GdScO_3$ and optimized Yb^{3+}, Er^{3+} co-doped $GdScO_3$ powder samples was analyzed using scanning electron microscopy (SEM) and high-resolution transmission electron microscopy (HR-TEM) with a Tecnai G2 20 TWIN 200 kV (FEI) system. TEM images of the $GdScO_3$ powder, shown in Fig. 6.3(a) and 6.3(b), verify the formation of $GdScO_3$ NCs through a self-propagating gel-combustion reaction. The images depict particles with varying sizes, generally exhibiting a tendency towards spherical shapes. The interplanar spacing (d-spacing) of the $GdScO_3$ NCs for the (101) plane is approximately 3.96 Å, as shown in Fig. 6.3(c). The elemental analysis of optimized Yb^{3+}, Er^{3+} co-doped $GdScO_3$ sample was conducted using SEM-energy dispersive X-ray analysis (EDX) with an EVO - Scanning Electron Microscope MA15/18, CARL ZEISS MICROSCOPY LTD, 51N1000 – EDS System. The EDX spectrum presented in Fig. 6.3(d) and atomic percentages of the elements obtained through EDX analysis are listed in the inset.

The spectrum consists of all elements peaks used for the synthesis confirms the presence of all the constituent elements in Yb^{3+}, Er^{3+} co-doped $GdScO_3$ sample.

Fig. 6.3(e) shows the selected area electron diffraction (SAED) pattern for $GdScO_3$ sample. The inner circle in the SAED pattern indexed to the (101) plane. In the SAED pattern next bigger circles are identified as the (111), and so on for (200), and (121) planes. The SAED pattern can be used to determine whether a material is crystalline or amorphous. In general, spots pattern in the SAED pattern are characteristic of monocrystalline materials, while the spots forming rings indicate polycrystalline materials or different crystallographic phases. In contrast, amorphous materials typically produce halo rings in the SAED pattern. Therefore, the observed SAED pattern confirms the crystalline nature of the synthesized sample. Both spots and rings in the diffraction patterns used for the calculation of the d-spacing for various crystal planes.

6.3.2 UV-visible NIR absorption analysis

The spectra of UV-visible-NIR absorption were recorded using a Shimadzu UV-2600 spectrophotometer within the wavelength range of 250-1200 nm. Fig. 6.4(a) illustrates the UV-visible NIR absorption spectra of as-synthesized $GdScO_3$, 0.5% Er^{3+}-doped $GdScO_3$, and 3.0% Yb^{3+} and 0.5% Er^{3+} co-doped $GdScO_3$ (optimized) powder samples. In the spectrum of optimized Yb^{3+}, Er^{3+} co-doped $GdScO_3$, four absorption peaks were observed at 275, 379, 521, and 980 nm. The peak around 275 nm is attributed to the high band gap characteristics of the host material [223]. The absorption peak at 379 nm corresponds to the transition from the $^4I_{15/2}$ to the $^4G_{11/2}$ level in Er^{3+}-ion, while the 521 nm peak is associated with the transition from $^4I_{15/2}$ to $^4H_{11/2}$ [224]. These 379 nm and 521 nm absorption peaks are also present in the PL excitation spectrum of the Er^{3+}-containing $GdScO_3$ powder

samples, as shown in Fig. 6.6(a). The absorption peak at 980 nm is characteristic absorption of the Yb^{3+}-ion, corresponding to the $^2F_{7/2} \rightarrow {}^2F_{5/2}$ transition, and is only observed after Yb^{3+}-ion is co-doped into the Er^{3+}-doped $GdScO_3$. The absorption spectrum of optimized Yb^{3+}, Er^{3+} co-doped $GdScO_3$ powder sample calcined at 1000 ºC is depicted in Fig. 6.4(b) The absorption spectra of both the as-synthesized and 1000 ºC calcined powder samples are nearly identical.

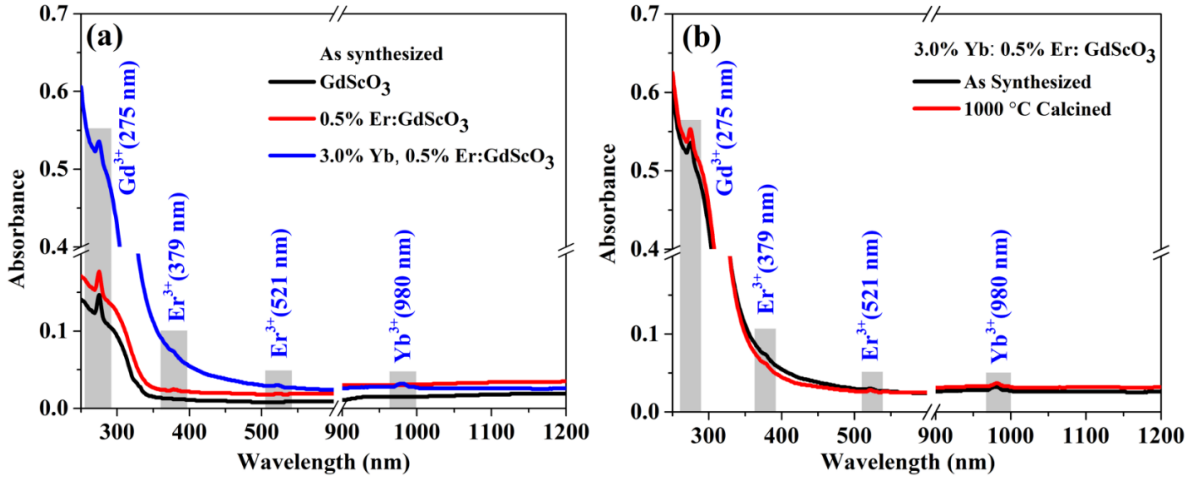

Figure 6.4: UV-visible absorption spectra of (a) as-synthesized pristine $GdScO_3$, 0.5% Er^{3+}-doped $GdScO_3$, and 3.0% Yb^{3+}, 0.5% Er^{3+} co-doped $GdScO_3$ powder sample, (b) as-synthesized and 1000 ºC calcined 3.0% Yb^{3+}, 0.5% Er^{3+} co-doped $GdScO_3$ powder sample.

6.3.3 Fourier Transform-Infared (FT-IR) analysis

The FT-IR spectra of the optimized Yb^{3+}, Er^{3+} co-doped $GdScO_3$ powder sample recorded using the Nicolet iS5 (ThermoFisher) in the wavenumber range of 400–4000 cm^{-1}. The spctra were analyzed to investigate the chemical composition and functional groups present. Fig. 6.5(a) and 6.5(b) displays the FT-IR spectra for both the as-synthesized and 1000 ºC heat-treated optimized Yb^{3+}, Er^{3+} co-doped $GdScO_3$ samples, respectively. The spectra exhibit characteristic peaks at approximately 412, 434, 450, 558, 1050, 1145, 1384, 1522, 1636, 2926, and 3432 cm^{-1}.

The broad absorption band observed at 3432 cm^{-1} is attributed to water molecule O-H stretching vibrations. The presence of carboxyl groups, which include both carbonyl (C=O) and hydroxyl (O-H) groups bonded to the carbon atom also contribute peak at 3432 cm^{-1} [225]. Upon heat treatment at 1000 ºC, the intensity of this peak decreases but does not vanish entirely [226][227]. The presence of a strong C=O stretching vibration after thermal treatment could be due to the adsorption of CO_2 and H_2O molecules from the air onto the sample surface [228]. The peak at approximately 2926 cm^{-1} corresponds to the symmetric and asymmetric vibrations of the CH_3 groups in alkenes [229]. The peaks at 1636, 1522, and 1384 cm^{-1} are associated with the stretching vibrations of hydroxyl groups and the asymmetric stretching of carbonate groups [230].

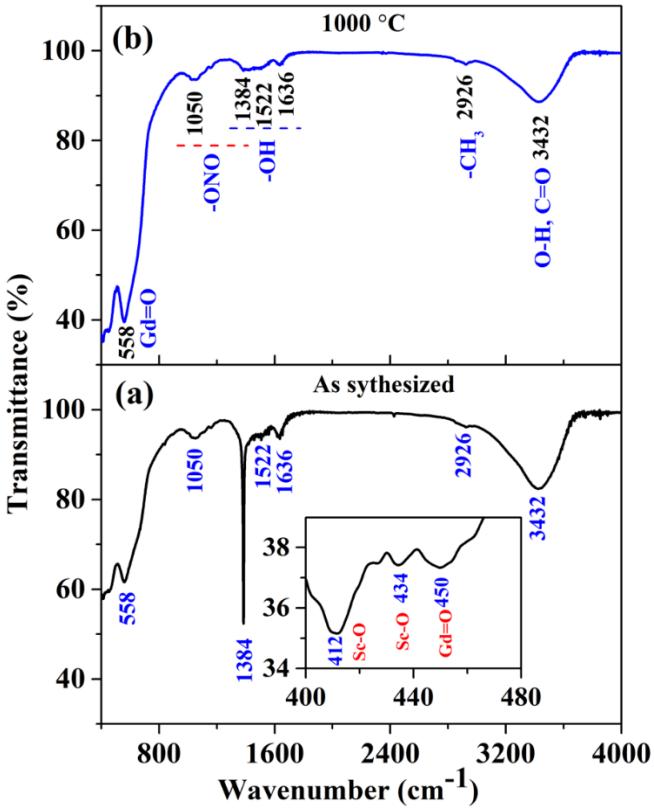

Figure 6.5: FT-IR spectra of (a) as-synthesized Yb^{3+}, Er^{3+}: $GdScO_3$ and, (b) 1000 ºC calcined Yb^{3+}, Er^{3+}: $GdScO_3$.

The presence of nitrate-ions in the sample is indicated by two peaks, a prominent one at 1384 cm^{-1} and a secondary one at 1050 cm^{-1} [225][231]. The former peak is linked to uncoordinated nitrate-ions, which diminish significantly after heat treatment at 1000 ºC, as seen in Fig. 6.5(b) [231]. The bands peaks centered at 558 and 450 cm^{-1} are attributed to Gd-O vibrations [225][232], while the peaks at 434 and 412 cm^{-1} are characteristic of Sc-O bonds, depicted in the inset of Fig. 6.5(a) [233]. The presence of these metal-oxygen vibrational peaks confirms the formation of the $GdScO_3$ phase, supporting the XRD results.

6.3.4 Photoluminescence (PL) excitation and emission study

The PL studies are crucial for assessing the optical properties of samples. The PL excitation and emission spectra were measured using a Horiba Fluorolog-3 spectrophotometer, which is equipped with a 450 W Xenon lamp as the light source and a photomultiplier tube (PMT) as the detector. The PL excitation spectrum of 0.5% Er^{3+}-doped $GdScO_3$, recorded for 525 nm emission is depicted in Fig. 6.6(a), while for the 547 nm emission is shown in the inset. Additionally, the PL excitation spectrum for 3.0% Yb^{3+}, 0.5% Er^{3+} co-doped $GdScO_3$ recorded by monitoring emission at 525 nm, is illustrated in Fig. 6.6(b). The major excitation peaks appear at 275, 379, and 521 nm. Notably, a prominent excitation peak at 379 nm corresponds to the transition from the $^4I_{15/2}$ to the $^4G_{11/2}$ level of Er^{3+}-ion [224].

The PL emission spectra of as-synthesized 0.5% Er^{3+}-doped $GdScO_3$ and 3.0% Yb^{3+}, 0.5% Er^{3+} co-doped $GdScO_3$ depicted in Fig. 6.6(c) and 6.6(d), respectively, were recorded by 379 nm excitation. The PL spectra exhibit emission peaks at 416, 525, 547, and 662 nm [26]. These peaks correspond to characteristic transitions from various excited states to the

$^4I_{15/2}$ level in Er^{3+}-ion.. Specifically, the peak at 416 nm is attributed to the $^2H_{9/2} \rightarrow {}^4I_{15/2}$ transition, the 525 nm peak to the $^2H_{11/2} \rightarrow {}^4I_{15/2}$ transition, the 547 nm peak to the $^4S_{3/2} \rightarrow {}^4I_{15/2}$ transition, and the 662 nm peak to the $^4F_{9/2} \rightarrow {}^4I_{15/2}$ transition. All these transitions involving Er^{3+}-ion are illustrated in the partial energy level diagram shown in Fig. 6.8(b).

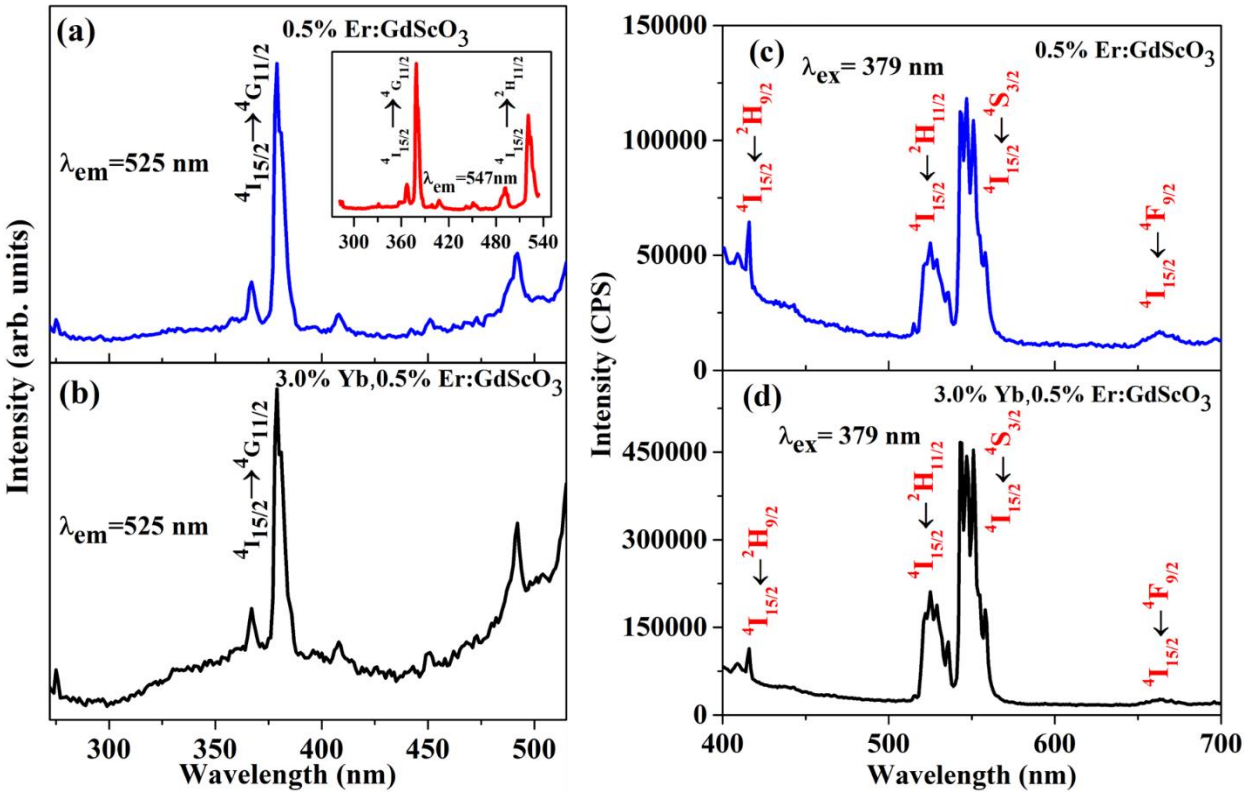

Figure 6.6: PL excitation spectrum of (a) $Er_{0.005}Gd_{0.995}ScO_3$ (inset: monitored emission at 547 nm), (b) $Yb_{0.03}Er_{0.005}Gd_{0.965}ScO_3$ for 525 nm emission. PL emission spectrum of (c) $Er_{0.005}Gd_{0.995}ScO_3$, (d) $Yb_{0.03}Er_{0.005}Gd_{0.965}ScO_3$ recorded by 379 nm excitation.

The PL emission spectra of the Yb^{3+}, Er^{3+} co-doped $GdScO_3$ for the varous Yb^{3+}-ion concentration is recorded to optimize the emission intensity. Also PL emission spectrum of as synthesized and 1000 °C calcined 3.0% Yb^{3+}, 0.5% Er^{3+} co-doped $GdScO_3$ are recorded, as presented in 6.7(b). Notably, the PL emission intensity of the calcined sample is approximately three times higher than that of the as-synthesized one. This increase in PL

intensity is likely due to improved crystallinity at higher calcination temperatures, which reduces inherent crystal defects [234].

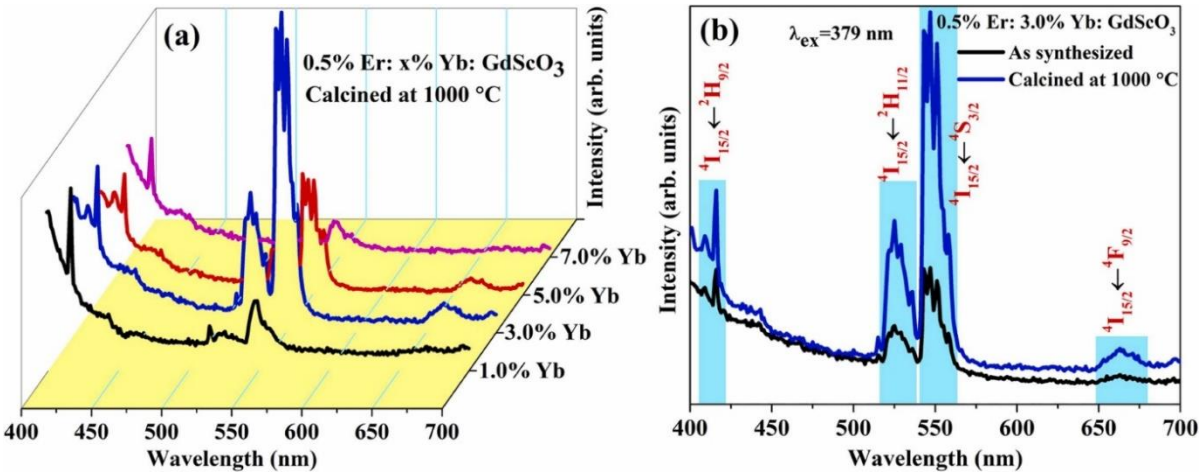

Figure 6.7: (a) PL emission spectra of $Yb_xEr_yGd_{1-x-y}ScO_3$, x=0.01, 0.03, 0.05, 0.07, and y=0.005 ($\boldsymbol{\lambda_{ex} = 379\ nm}$), (b) PL emission spectra of as-synthesized and 1000 ºC calcined 3.0% Yb^{3+}, 0.5% Er^{3+}: $GdScO_3$ ($\boldsymbol{\lambda_{ex} = 379\ nm}$).

The PL emission spectra of $Yb_xEr_yGd_{1-x-y}ScO_3$; x=0.01, 0.03, 0.05, and 0.07 with fixed y=0.005 are illustrated in Fig. 6.7(a). As the Yb^{3+}-ion doping concentration increases, there is an initial rise in the intensity of the PL emission peaks. This is attributed to the enhanced energy transfer efficiency from senitizer Yb^{3+} to activator ion Er^{3+}. The optimal Yb^{3+} doping concentration in $Yb_xEr_yGd_{1-x-y}ScO_3$ is found to be 3.0% for fixed 0.5% Er^{3+}, corresponding to the high emission intensity among the other. However, when the Yb^{3+} doping concentration exceeds 3.0%, the emission peak intensity diminishes due to concentration quenching. At higher doping levels, the increased proximity of atoms around the luminescence center likely facilitates non-radiative energy transfer to nearby atoms. This leads to the energy dissipation via thermionic and phonon absorption processes.

6.3.5 Photons Upconversion (UC) study

The photon UC is a non-linear optical process where the sequential absorption of two or more low energy infrared (IR) photons results in the emission of high energy visible or ultraviolet (UV) photons. Unlike two-photon absorption (TPA) and second harmonic generation (SHG) processes, where energy levels involved are virtual, the energy levels in UC processes are real. The Yb^{3+}-ion, commonly used as sensitizer, is often co-doped with activators such as Er^{3+}, Ho^{3+}, or Tm^{3+}-ion containing host materials for UC emission [235]. In this work, UC emission in Yb^{3+}, Er^{3+} co-doped $GdScO_3$ was reported first time. The UC study was conducted using a Fluorolog-3 photoluminescence spectrometer setup. The setup integrated with a 980 nm continuous wave (CW) diode laser with a tunable power output of 2.2 W as the excitation source. In photon UC process, Yb^{3+}-ion absorb 980 nm IR photons and transfer the energy to the activator ions Er^{3+}. It was observed that the intensity of the UC emission peaks was higher for the sample calcined at 1000 ºC, consistent with the PL emission spectra. The UC spectra of optimized Yb^{3+}, Er^{3+} co-doped $GdScO_3$ powder samples calcined at 1000 ºC are presented in Fig. 6.8(a). The laser light of wavelength 980 nm with 739 mW power irradiated on the sample an area of approximately 0.3 cm^2. The recorded UC spectra for $Yb_xEr_yGd_{1-x-y}ScO_3$; x=0.01, 0.03, 0.05, and 0.07 with fixed y=0.005, are shown in Fig. 6.8(a).

In the UC mechanism in Yb^{3+}-Er^{3+}-ions pair, the IR photons from the 980 nm laser absorbed by the Yb^{3+}-ion to the $^2F_{5/2}$ level [236]. Then Yb^{3+}-ion transfer energy non-radiatively from the $^2F_{7/2}$ level to the $^4I_{11/2}$ level of Er^{3+}-ion. Additionally, the $^4I_{11/2}$ level of Er^{3+}-ion can be directly populated through ground state absorption (GSA) of the 980 nm photons. Most of the ions relax from the $^4I_{11/2}$ to the $^4I_{13/2}$ level. The absorption of a second

photon via the excited state absorption (ESA) process then occurs in the $^4I_{13/2}$ and $^4I_{11/2}$ levels, populating the $^4F_{9/2}$ and $^4F_{7/2}$ levels, respectively. Additionally, the $^4F_{7/2}$ level of the Er^{3+}-ion can also be populated through cooperative energy transfer (CET) involving simultaneous energy transfer from two excited Yb^{3+}-ions.

The UC emission spectra of Yb^{3+}, Er^{3+} co-doped $GdScO_3$ consists peaks at 525, 547, and 662 nm. The 525 nm emission peak results from the $^2H_{11/2} \rightarrow {}^4I_{15/2}$ transition, the 547 nm from the $^4S_{3/2} \rightarrow {}^4I_{15/2}$ transition, and the 662 nm from the $^4F_{9/2} \rightarrow {}^4I_{15/2}$ transition in Er^{3+}-ion, as shown in Fig. 6.8(b). The 662 nm peak emerges after the incorporation of Yb^{3+} ions in Er^{3+}-doped $GdScO_3$ depicted in Fig. 6.8(a). The intensity of UC emission peaks initially increases, reaching a maximum at 3.0% Yb^{3+} doping in x% Yb^{3+}, 0.5% Er^{3+}: $GdScO_3$, indicating this is the optimized Yb^{3+} doping concentration for high UC emission intensity.

For the optimized doping concentration, the intensities of the 547 nm and 662 nm peaks are nearly same. Beyond this optimal concentration, the overall peak intensity decreases. Below the optimized doping concentration, the green emission band intensity is higher than the red band, while above it, the red emission band intensity surpasses the green.

At higher Yb^{3+} concentration, the ions relaxation from the $^4I_{11/2}$ to the $^4I_{13/2}$ level becomes more prominent than the transfer of ions from the $^4I_{11/2}$ to the $^4F_{7/2}$ level. This could be due to the ions population in the $^4I_{11/2}$ level exceeding a threshold, leading to a greater population of the $I_{13/2}$ level compared to the $^4F_{7/2}$ level, resulting in a higher red emission intensity than green in UC emssion. However, the overall UC emission intensity increases up to 3.0% Yb^{3+} doping, beyond this intensity decreases.

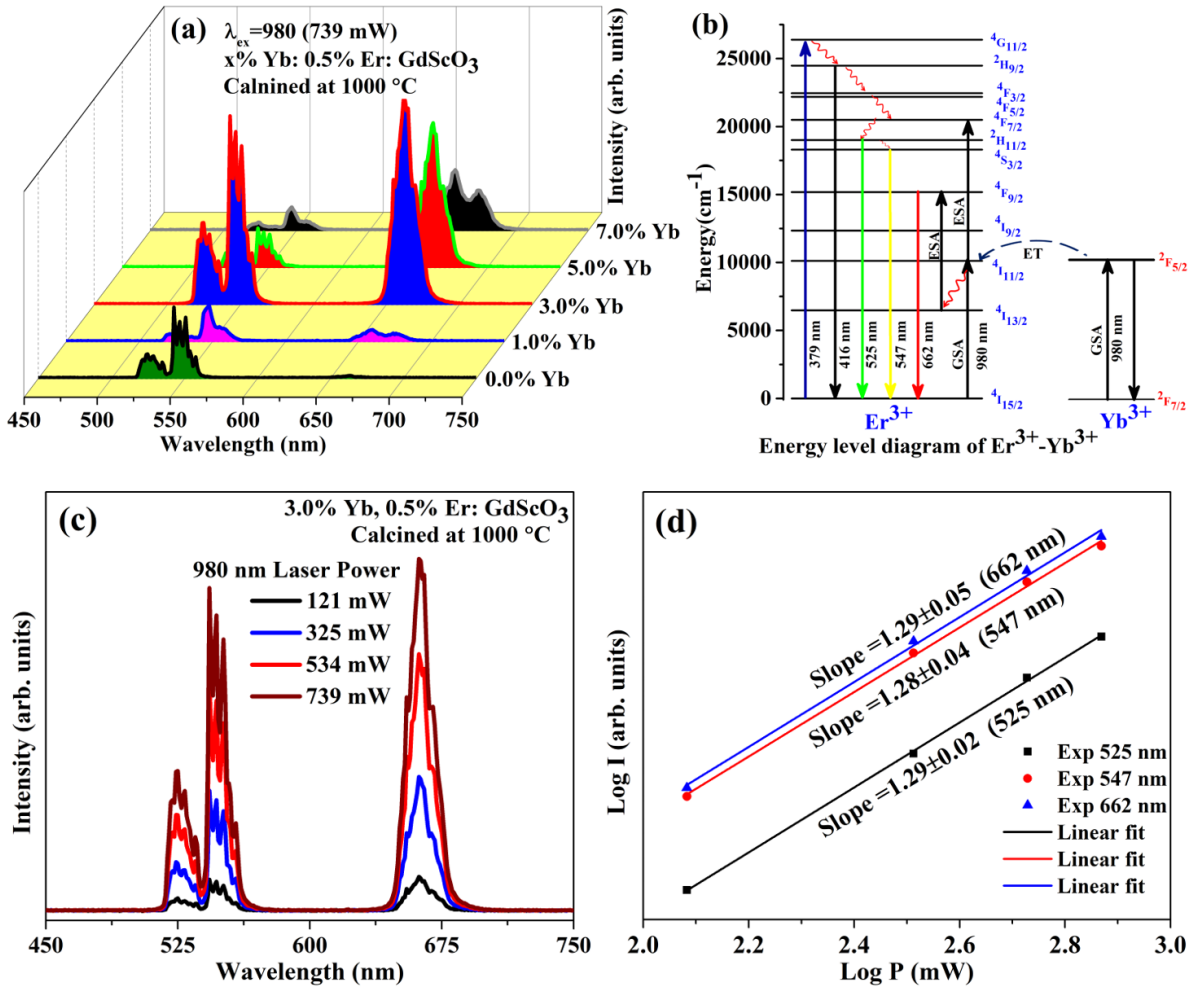

Figure 6.8: (a) UC emission spectra of $Yb_xEr_yGd_{1-x-y}ScO_3$, x=0.00, 0.01, 0.03, 0.05, and 0.07 with fixed y=0.005, (b) partial energy level diagram of Er^{3+}-Yb^{3+}, (c) UC emission spectra of $Yb_{0.03}Er_{0.005}Gd_{0.965}ScO_3$ at different excitation power of 980 nm CW laser, (d) Log-log plot of $Yb_{0.03}Er_{0.005}Gd_{0.965}ScO_3$ UC emission peaks intensity.

The excitaion laser power-dependent UC spectra of the optimized Yb^{3+}, Er^{3+} co-doped $GdScO_3$ sample are depicted in Fig. 6.8(c). As the laser excitation power increases, the intensity of the UC emission peaks also rises. The relationship between the UC emission peak intensity and the laser excitaion power is governed by the equation $I \propto P^n$; where I represents the peak intensity, P is the laser excitaion power, and n indicates the number of photons involved in generating a single visible photon through the UC process. The log-log plot of I versus P is shown in Fig. 6.8(d). This, give n values of 1.29 ± 0.02, 1.28 ± 0.04, and 1.29 ± 0.05 for the emission peaks at 525, 547, and 662 nm, respectively. These values align

well with previously reported data [237], suggesting a two-photon process involve in the UC emission. The fact that the obtained *n* values are slightly less than 2 may be attributed to energy losses during the UC process [238]. Additionally, the reduction in *n* can be explained by ions cross-relaxation among different energy levels [237]. Some ions from the $^4F_{9/2}$ level transition to the $^4S_{3/2}$ and $^4I_{9/2}$ levels, reducing the population of the $^4F_{9/2}$ level. Back-transfer of ions from the $^4F_{9/2}$ to the $^4S_{3/2}$ level is another potential mechanism contributing to the reduced *n* value. A similar mechanism is likely happen for the the $^2H_{11/2}$ and $^4S_{3/2}$ levels. The intense laser light can also induce saturation effects on the thermally coupled levels, result in the decreased *n* value from 2.

6.3.6 Commission International de I′ Eclairage (CIE) Chromaticity study

The CIE 1931 chromaticity coordinate diagram for 0.5% Er^{3+}-doped $GdScO_3$ and 3.0% Yb^{3+}, 0.5% Er^{3+} co-doped $GdScO_3$ is depicted in Fig. 6.9 for both downconversion (DC) and UC emission.

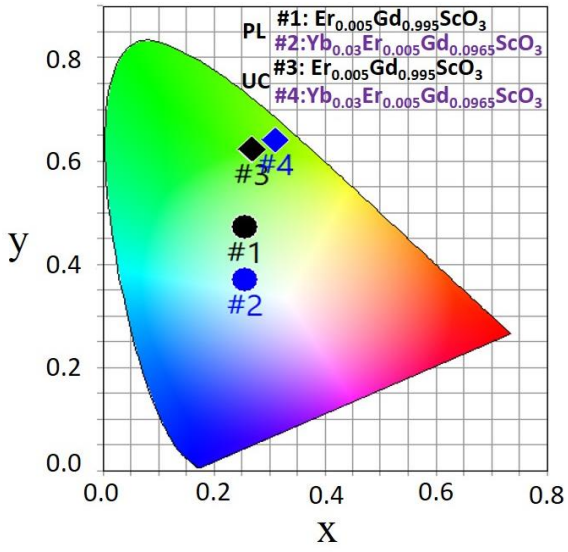

Figure 6.9: CIE 1931 chromaticity diagram of the $Er_{0.005}Gd_{0.995}ScO_3$ (#1), $Yb_{0.03}Er_{0.005}Gd_{0.965}ScO_3$ (#2) for the DC emission. CIE 1931 chromaticity diagram of the $Er_{0.005}Gd_{0.995}ScO_3$ (#3), and $Yb_{0.03}Er_{0.005}Gd_{0.965}ScO_3$ (#4) for the UC emission.

The color (x, y) coordinates for of 0.5% Er^{3+}-doped $GdScO_3$ and 3.0% Yb^{3+}, 0.5% Er^{3+} co-doped $GdScO_3$ in DC mode are (0.256, 0.472) (#1) and (0.257, 0.369) (#2), respectively. In UC mode, the coordinates shift to (0.269, 0.623) (#3) and (0.311, 0.641) (#4), respectively for the 0.5% Er^{3+}-doped $GdScO_3$ and 3.0% Yb^{3+}, 0.5% Er^{3+} co-doped $GdScO_3$. This indicates that the emission color can be tuned by doping concentration of Yb^{3+} ions and by the excitation wavelength [217]. Additionally, the luminous efficacy of optical radiation (LER), which quantifies how effectively light is perceived by the human eye, was measured [239][240]. For 0.5% Er^{3+}-doped $GdScO_3$, the LER values in UC and DC modes are 375 lm/W and 517 lm/W, respectively. Meanwhile, for 3.0% Yb^{3+}, 0.5% Er^{3+} co-doped $GdScO_3$, the LER values are 280 lm/W in UC mode and 340 lm/W in DC mode.

6.4 Temperature-dependent UC and optical temperature sensing

Temperature measurement/monitoring has become increasingly vital not only for the well-being of humans and other living organisms but also for industrial and scientific operations. In the materials processing industry, even minor deviations from the optimal temperature can result in imperfections. Traditionally, temperature monitoring devices like thermometers, thermocouples, and resistive temperature measurement instruments are widely utilized. However, these are contact-based measurement, which are unsuitable in situations where direct contact with the specimen is difficult or impossible; such as in coal mine fires, high-temperature material processing, or volcanic eruptions. In such scenarios, non-contact temperature sensors are crucial for assessing the thermal conditions of distant objects. After observing the effective optical response of Yb^{3+}, Er^{3+} co-doped $GdScO_3$, we have investigated its potential for the luminescence-based non-contact temperature sensing.

The temperature-dependent UC emission spectra mesurement of optimized Yb^{3+}, Er^{3+} co-doped $GdScO_3$ powder was conducted over a temperature range of 299 K to 473 K, utilizing 980 nm CW laser as excitation source. An external homemade heater, regulated by a variac, was employed to control the temperature. The UC emission was collected via optical fiber and directed into a PMT based detctor. A thermocouple was strategically placed near the laser-illuminated spot on the sample to accurately monitor the sample's temperature and ensure minimal temperature gradient during measurements. The variation in intensity of the UC emission peaks at 525 and 547 nm as a function of temperature is depicted in Fig. 6.10(a). The emission intensity change given as according to the Arrhenius equation;

$$I_T = \frac{I_0}{1 + B\exp\left(\frac{-E_a}{k_B T}\right)} \quad \ldots (6.2)$$

The peak intensities at temperature *T* and the initial (room) temperature are represented by I_T and I_0, respectively. The parameter *B* denotes the quenching frequency factor, E_a is the activation energy, and k_B is the Boltzmann constant. A lower activation energy corresponds to a higher probability of non-radiative transitions, which in turn leads to reduced material stability.

The $^2H_{11/2}$ and $^4S_{3/2}$ of the Er^{3+}-ion are thermally coupled levels. In thermal equilibrium, the ions population in these level is determind by the Boltzmann's distribution law. The intensity of the 525 nm peak assigned to the $^2H_{11/2} \rightarrow {}^4I_{15/2}$ transition, increases with temperature up to 398 K, after this temperrature its intensity decrease, as illustrated in Fig. 6.10(b). In contrast, the intensity of the 547 nm peak, corresponding to the $^4S_{3/2} \rightarrow {}^4I_{15/2}$ transition, consistently decreases with increasing temperature.

Initially, ESA process from the $^4I_{11/2}$ level is thermally assisted, leading to population of the $^4F_{7/2}$ level. Subsequently, non-radiative relaxation from the $^4F_{7/2}$ level to the $^2H_{11/2}$ level occurs, which results in an increase in the intensity of the emission peak cooresponing to the $^2H_{11/2} \rightarrow {}^4I_{15/2}$ transition. However, at higher temperatures, electron-phonon interactions become more effective, causing energy dissipation and leading to a decrease in UC emission intensity. The overall emission intensity decreases with increasing temperature, primarily due to thermal quenching, which can be described by the Arrhenius equation (equation 6.2) [241]. Additionally, at elevated temperatures, non-radiative recombination processes become more dominant, further reducing the emission intensity [242]. Notably, the sample does not exhibit significant emission peak shifts or peak broadening with increasing temperature, indicating that electron-phonon scattering in this material is minimal [242].

According to Boltzmann's distribution law, the fluorescence intensity ratio (FIR) of the thermally coupled levels emission peaks is given as

$$FIR = \frac{I_H}{I_S} = Aexp\left(\frac{-\Delta E}{k_B T}\right) \quad \ldots (6.3)$$

Here, I_H and I_S represent the emission peaks intensities of the transitions $^2H_{11/2} \rightarrow {}^4I_{15/2}$(525 nm) and $^4S_{3/2} \rightarrow {}^4I_{15/2}$ (547 nm), respectively in Er^{3+}-ion. These intensities are directly proportional to the population densities of the corresponding energy states from which the transitions occur. The term A is a constant, and ΔE denotes the energy separation between the thermally coupled levels, which is determined from the slope of the (*FIR*) vs. 1/T plot. Here, k_B represents Boltzmann's constant, and T is the absolute temperature. Th FIR of UC emission spectra of the optimized Yb^{3+}, Er^{3+} co-doped $GdScO_3$ sample were recorded over the temperature range from 299 K to 473 K, as depicted in Fig. 6.10(a).

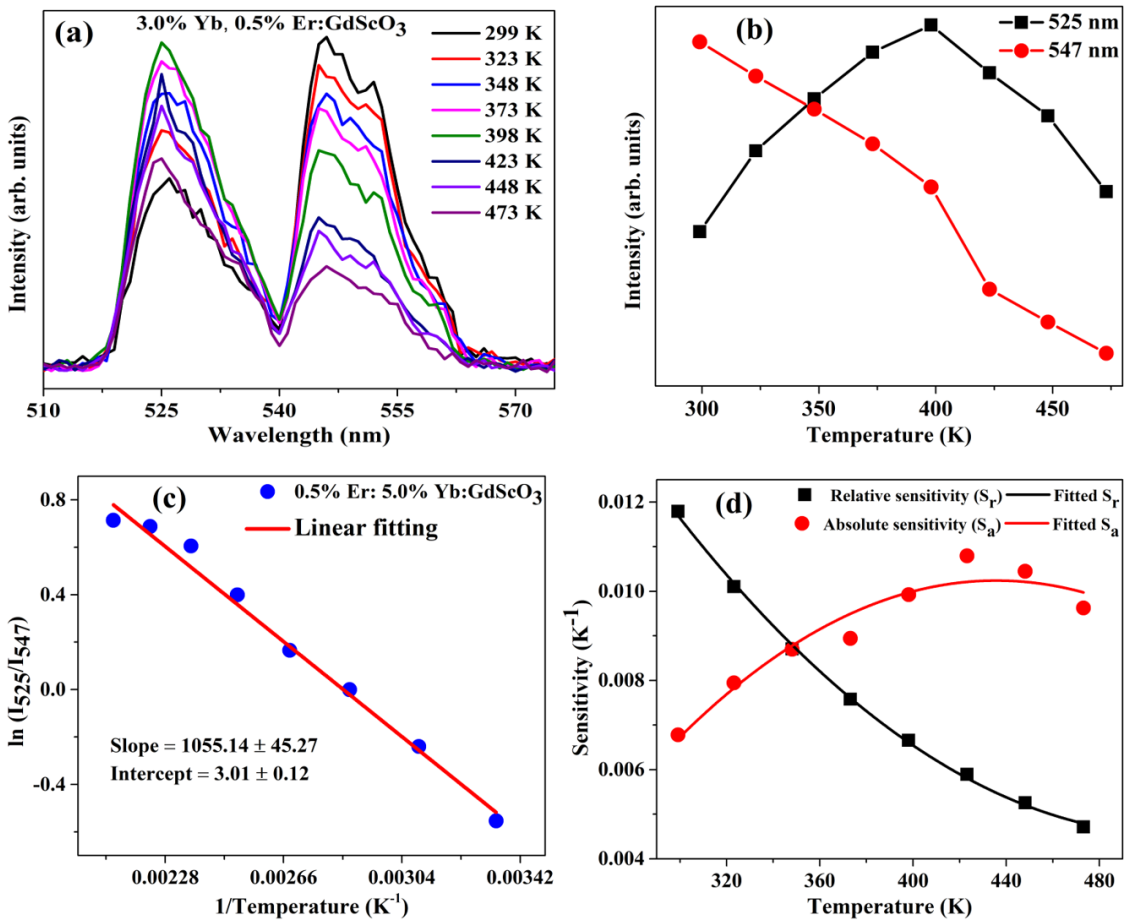

Figure 6.10: (a) Temperature dependent UC emission spectra of $Yb_{0.03}Er_{0.005}Gd_{0.965}ScO_3$, (b) 525 nm and 547 nm UC emission peaks intensity at different temperatures. (c) Ln (FIR) vs. 1/T (K^{-1}) plot, (d) relative and absolute sensitivity of the $Yb_{0.03}Er_{0.005}Gd_{0.965}ScO_3$ powder sample.

The FIR value increases from 0.575 to 2.042 as the temperature rises from 299 K to 473 K, beyond which the signal-to-noise ratio of the UC emission becomes too low for reliable measurements. To determine ΔE, equation (6.3) was adjusted, and a plot of ln(*FIR*) against (1/T) is presented in Fig. 6.10(c).

$$\ln(FIR) = \left(\frac{-\Delta E}{k_B T}\right) + \ln(A) \qquad \ldots (6.4)$$

The slope of this plot, when multiplied by k_B, yields ΔE value, while the intercept gives ln(*A*). The slope and intercept values were found to be 1055.14 ± 45.27 and 3.01 ± 0.12, respectively. The calculated ΔE from the graph is approximately 733.41 cm^{-1}, which closely

aligns with the ΔE value of 766 cm^{-1} obtained from the emission peaks of thermally coupled levels.

The effectiveness of the temperature sensor is determined by two key parameters: absolute sensitivity (S_a) and relative sensitivity (S_r). For optimal sensor performance, these values should be as high as possible. The S_a is defined as the rate of change of the FIR with temperature, and is given by [243];

$$S_a = \frac{d(FIR)}{dT} = FIR \times \frac{\Delta E}{k_B T^2} \quad \ldots (6.5)$$

For the comparative study of sensitivity in different host, S_r is an important over S_a. The S_r compares the change in the FIR to the intensity ratio itself, mathematically it is expressed as;

$$S_r = \left(\frac{1}{FIR}\right) \times \frac{d(FIR)}{dT} = \frac{\Delta E}{k_B T^2} \quad \ldots (6.6)$$

The symbols in equations (6.5) and (6.6) retain their usual meanings as previously defined. The maximum S_a value achived in Yb^{3+}, Er^{3+} co-doped $GdScO_3$ is $(10.49 \pm 0.04) \times 10^{-3}$ K^{-1} at 423 K. The highest S_r value obtanined is $(11.790 \pm 0.008) \times 10^{-3}$ K^{-1} at 299 K. The thermal resolution (ΔT) achieved in this sample is 0.4 K, which quanlifies the smallest detectable temperature difference by the sample [244].

$$\Delta T = \Delta \mathrm{FIR} \times \frac{k_B T^2}{FIR \times \Delta E} = \frac{\Delta\{\ln(FIR)\}}{S_r} \quad \ldots (6.7)$$

There is extensive literature on temperature sensing applications involving Ln^{3+}-doped oxide-based materials of various types [245][246][247][248][249][250]. For sensitivity comparison, either the host material or the dopant ions should be same. The S_a and S_r value of Er^{3+} containing oxide-type perovskite (ABO_3) reported, were compared with the sensitivity observed in Yb^{3+}, Er^{3+} co-doped $GdScO_3$ sample and listed in Table 6.2.

Table 6.2 Optical temperature sensing parameters of Ln^{3+}-doped oxide perovskite (ABO_3; A, and B are metal cations).

Metal-ion: ABO_3	**Temperature range (K)**	**Maximum relative sensitivity (S_r) (K^{-1})**	**Maximum absolute sensitivity (S_a) (K^{-1})**
Er^{3+}, Yb^{3+}:$CaTiO_3$	303-523	11.65×10^{-3} at 303 K	9.43×10^{-3} at 473 K[251]
Er^{3+}, Yb^{3+}, Na^{+}:$CaTiO_3$	303-523	10.87×10^{-3} at 303 K	8.02×10^{-3} at 453 K [251]
Er^{3+}, Yb^{3+}, Li^{+}:$CaTiO_3$	303-523	12.17×10^{-3} at 303 K	10.03×10^{-3}at 513 K [251]
Er^{3+}, Yb^{3+}, Nd^{+}:$CaTiO_3$	303-573	10.90×10^{-3} at 303 K	8.8×10^{-3} at 508 K [244]
Er^{3+}, Yb^{3+}:$BaTiO_3$	120-505	-	1.92×10^{-3} at 410 K [237]
Er^{3+}, Yb^{3+}, Zn^{2+}:$BaTiO_3$	120-505	-	4.75×10^{-3} at 430 K [237]
Er^{3+}, Yb^{3+}: $LiNbO_3$	285-453	-	7.7×10^{-3} at 310 K [252]
Er^{3+}:$PbTiO_3$	333-493	8.73×10^{-3} at 333 K	3.1×10^{-3} at 475 K [253]
Er^{3+}, Yb^{3+}: $PbTiO_3$	298-548	12.25×10^{-3} at 298 K	5.54×10^{-3} at 548 K [254]
Er^{3+}, Yb^{3+}: $LaAlO_3$	100-673	24.4×10^{-3} at 175 K	4.8×10^{-3} at 400 K [255]
Er^{3+}: $LaGdO_3$	283-393	12.7×10^{-3} at 283 K	3.1×10^{-3} at 393 K [256]
Er^{3+}, Yb^{3+}: $LaGdO_3$	283-393	10.8×10^{-3} at 283 K	3.4×10^{-3} at 393 K [256]
Er^{3+}, Nd^{3+}: $GdScO_3$	80-743	9.6×10^{-3} at 300 K	- [257]
Er^{3+}, Yb^{3+}: $GdScO_3$	299-473	11.79×10^{-3} at 299 K	10.49×10^{-3} at 423 K*

*Present work.

Table 6.2 demonstrates that the S_r and S_a value of the Yb^{3+}, Er^{3+}: $GdScO_3$ are efficient for temperature sensing application compared to other reported oxide-perovskites. The S_r value is moderate among Ln^{3+}-doped oxide perovskites. However, the S_a value is the highest among the listed Ln^{3+}-doped oxide perovskites. These exceptional properties of Yb^{3+}, Er^{3+} co-doped $GdScO_3$ identified it as a promising material for future luminescence-based optical temperature sensing applications.

6.5 Conclusions

In summary, in this Chapter, the successful synthesis of high bandgap pristine $GdScO_3$ and Yb^{3+}, Er^{3+} co-doped $GdScO_3$ NCs using self-propagarted gel combustion method were done at low temperatures. The doping concentrations Yb^{3+}-ions was optimized for the high luminescence intensity. This material exhibits strong NIR-to-visible UC emission under 980 nm laser excitation, as well as down-shifting emission when excited by UV-blue light. To the best of our knowledge, this was the first report on UC emission in Yb^{3+}, Er^{3+} co-doped $GdScO_3$. The sample demonstrates a remarkable temperature-dependent response in UC emission, which has been utilized for temperature sensing application. The material achieves maximum absolute and relative sensitivity values of 10.49×10^{-3} K^{-1} at 423 K and 11.79×10^{-3} K^{-1} at 299 K, respectively, with a thermal resolution of 0.4 K. These sensitivity values surpass those of many reported oxide perovskite materials. This makes the material a promising candidate for non-contact, luminescence-based optical thermometry, particularly in environments like coal mines and high-temperature metal industries. Additionally, it has potential applications in the optoelectronic industry for monitoring heat-induced damage in electronic circuits.